Article

Transcranial volumetric imaging using a conformal ultrasound patch

Sai Zhou[1,9], Xiaoxiang Gao[2,9], Geonho Park[2,9], Xinyi Yang[1,9], Baiyan Qi[1], Muyang Lin[2], Hao Huang[2], Yizhou Bian[2], Hongjie Hu[2], Xiangjun Chen[1], Ray S. Wu[2], Boyu Liu[2], Wentong Yue[2], Chengchangfeng Lu[3], Ruotao Wang[2], Pranavi Bheemreddy[3], Siyu Qin[3], Arthur Lam[4], Keith A. Wear[5], Michael Andre[6], Erik B. Kistler[6,7], David W. Newell[8] & Sheng Xu[1,2,3,6,7 ✉]

Accurate and continuous monitoring of cerebral blood flow is valuable for clinical neurocritical care and fundamental neurovascular research. Transcranial Doppler (TCD) ultrasonography is a widely used non-invasive method for evaluating cerebral blood flow[1], but the conventional rigid design severely limits the measurement accuracy of the complex three-dimensional (3D) vascular networks and the practicality for prolonged recording[2]. Here we report a conformal ultrasound patch for hands-free volumetric imaging and continuous monitoring of cerebral blood flow. The 2 MHz ultrasound waves reduce the attenuation and phase aberration caused by the skull, and the copper mesh shielding layer provides conformal contact to the skin while improving the signal-to-noise ratio by 5 dB. Ultrafast ultrasound imaging based on diverging waves can accurately render the circle of Willis in 3D and minimize human errors during examinations. Focused ultrasound waves allow the recording of blood flow spectra at selected locations continuously. The high accuracy of the conformal ultrasound patch was confirmed in comparison with a conventional TCD probe on 36 participants, showing a mean difference and standard deviation of difference as -1.51 ± 4.34 cm s^{-1}, -0.84 ± 3.06 cm s^{-1} and -0.50 ± 2.55 cm s^{-1} for peak systolic velocity, mean flow velocity, and end diastolic velocity, respectively. The measurement success rate was 70.6%, compared with 75.3% for a conventional TCD probe. Furthermore, we demonstrate continuous blood flow spectra during different interventions and identify cascades of intracranial B waves during drowsiness within 4 h of recording.

Cerebral blood flow supplies oxygen and energy substrates and removes metabolic wastes to maintain proper brain functions. Continuous monitoring of cerebral haemodynamics enables screening and diagnosing brain disorders[2] as well as understanding neurovascular functions[3]. However, assessment of cerebral blood flow is challenging because cerebral vasculature is embedded deep inside the brain and protected by the skull. Various modalities to measure cerebral blood flow have been explored (Extended Data Table 1 and Supplementary Discussion 1), including positron emission tomography[4], computed tomography[5] and magnetic resonance imaging[6], which all provide adequate spatial resolution but require bulky equipment that prohibits continuous use. Emerging thermal[7], electrical[8], and optical probes[9] can be miniaturized for continuous monitoring, but these probes cannot provide sufficient spatiotemporal resolutions.

Transcranial Doppler (TCD) is widely used for cerebral haemodynamic monitoring because of its safety, low cost, portability, versatility and relatively high spatiotemporal resolutions (Supplementary Table 1). However, conventional TCD probes have several limitations. First, these probes are rigid and need to be manually held by well-trained clinicians or affixed using bulky headsets for continuous monitoring[1]. Slight misalignment between the ultrasound beam and the target vessel, often caused by hand movement, poor headset fastening or movement by the participant, can cause fluctuation, degradation or complete loss of signals[2]. Therefore, the headset is usually very tight, causing discomfort, thus limiting the typical recording time to less than 30 min (ref. 10). Second, these probes usually use a single transducer or a linear array of transducers, which can only image part of the intricate three-dimensional (3D) network of cerebral arteries. Different operators may acquire signals from different segments of the 3D network, affecting repeatability and reproducibility[1] (Extended Data Fig. 1). Furthermore, manual probe tilting is required to identify the optimal angle for the acquisition of high-quality spectra, a routine process that is both time-consuming and heavily reliant on the expertise of the operator. To address these problems, volumetric imaging can be used to guide

[1]Materials Science and Engineering Program, University of California San Diego, La Jolla, CA, USA. [2]Department of Nanoengineering, University of California San Diego, La Jolla, CA, USA. [3]Department of Electrical and Computer Engineering, University of California San Diego, La Jolla, CA, USA. [4]Department of Anesthesiology and Critical Care, University of California San Diego, La Jolla, CA, USA. [5]U.S. Food and Drug Administration, Silver Spring, MD, USA. [6]Department of Radiology, University of California San Diego, La Jolla, CA, USA. [7]Shu Chien-Gene Lay Department of Bioengineering, University of California San Diego, La Jolla, CA, USA. [8]Department of Neurosurgery, Seattle Neuroscience Institute, Seattle, WA, USA. [9]These authors contributed equally: Sai Zhou, Xiaoxiang Gao, Geonho Park, Xinyi Yang. ✉e-mail: shengxu@ucsd.edu

target selection (Supplementary Fig. 1). Although two-dimensional (2D) matrix arrays can provide volumetric imaging, currently these probes have limited spatiotemporal resolutions because of technical barriers in probe fabrication and data acquisition[11,12] (Supplementary Discussion 1).

Wearable ultrasound devices enable comfortable contact with the skin surface for sensing physiological signals in deep tissues[13–17]. However, probing inside the brain is challenging because of the strong signal attenuation (Supplementary Fig. 2 and Supplementary Discussion 2) and phase aberration (Supplementary Fig. 3 and Supplementary Discussion 3) caused by the skull. Furthermore, existing wearable ultrasound devices provide only one-dimensional (1D) signals[18], 2D images[19] or 3D images by inaccurate integration and extrapolation of multiple 2D image slices[20]. Here we report the first conformal ultrasound patch for accurate and continuous monitoring of cerebral blood flow in 3D (Supplementary Discussion 4). We use low-frequency ultrasound waves to reduce the skull-induced signal attenuation and phase aberration[21]. We add a copper mesh shielding layer to the device and adopt an ultrafast imaging technique to insonate the entire 3D region, which substantially improves the signal-to-noise ratio[22,23]. This technology represents a powerful platform for both clinical and fundamental haemodynamic studies.

Device design and characterizations

To minimize acoustic attenuation and phase aberration, four transcranial windows (temporal, orbital, submandibular and suboccipital) are commonly used for TCD[24] (Supplementary Fig. 4). These windows are relatively small (about 5 cm^2 in adults)[1], requiring a compact device design. By contrast, the cerebral arterial network has several major components, including the anterior cerebral arteries (ACA), middle cerebral arteries (MCA), posterior cerebral arteries (PCA), ophthalmic arteries, internal carotid arteries (ICA), basal artery and vertebral arteries (Supplementary Discussion 5). Most of these arteries are deep (around 40–100 mm) and widely distributed inside the brain[1] (Fig. 1a), requiring devices with a wide ultrasound field (Supplementary Fig. 5). Therefore, we used diverging waves to image the entire arterial network and focused waves to monitor local blood flow spectra at target arterial sections (Fig. 1b and Methods). Diverging waves extend the ultrasound field from a limited acoustic window (12 mm × 12 mm) to a much larger region (about 60 mm × 60 mm at 50 mm depth in this work), which allows for simultaneous insonation of multiple cerebral arteries. Focused waves minimize unnecessary ultrasound exposure to surrounding tissues for long-term monitoring of blood flow spectra.

We built a 16 × 16 matrix array with a 750-μm pitch and a 2-MHz centre frequency (Methods and Supplementary Discussion 6). The choice of such a low frequency reduces signal attenuation and phase aberration and thus enhances transcranial penetration depth[1] (Supplementary Discussions 2 and 3). The pitch is comparable to the ultrasound wavelength (that is, 770 μm in soft tissues at 2 MHz), enabling a large tilting angle of the ultrasound beam in 3D (Supplementary Fig. 6). The matrix array has an aperture of 12 mm × 12 mm, similar to that of established TCD probes[25,26], which enables insonation through the skull and focusing on deep targets[12]. Five layers of serpentine interconnections are used to address the 256 elements individually (Fig. 1a and Supplementary Fig. 7). The matrix array has excellent properties such as high electromechanical coupling coefficient, and negligible crosstalk, resulting in high sensitivity to Doppler shift (Methods and Supplementary Fig. 8). We designed a serpentine copper mesh as an electromagnetic shielding layer, which increased the signal-to-noise ratio on average by 5 dB (Methods and Supplementary Fig. 8). Encapsulation of the entire device by silicone elastomer allows for electrical insulation and conformal contact on various surfaces (Fig. 1c, Supplementary Figs. 9 and 10). The final device is 1.3 mm thick, 20 mm wide and 28 mm long, with a total weight of 0.945 g.

The ultrasound intensity of the device was measured in a water tank (Methods, Extended Data Fig. 2 and Supplementary Discussion 7). We limited the maximum derated mechanical index and derated spatial peak temporal average intensity of all ultrasound transmissions in this work to about 0.7 and 370 mW cm^{-2}, respectively. These values are well below the Food and Drug Administration Track 1 maximum recommended levels for TCD applications (that is, 1.9 and 720 mW cm^{-2}, respectively)[27]. After penetrating through a temporal bone specimen, the measured maximum derated spatial peak temporal average intensity was reduced by approximately 83% to about 63 mW cm^{-2} (Extended Data Fig. 2 and Supplementary Fig. 11). For orbital window scans, the maximum mechanical index and derated spatial peak temporal average intensity were reduced to conform to the Food and Drug Administration Track 1 recommended maximum levels for ophthalmic scans (0.23 and 17 mW cm^{-2}, respectively)[27].

To characterize its thermal effect, we attached the device to the scalp of a normal human volunteer and activated the device for 4 h. The maximum temperature rise on the skin surface was less than 1 °C (Supplementary Fig. 12). Furthermore, for estimated temperature changes of internal tissues during prolonged ultrasound exposure, we calculated the thermal index[27], the ratio between the incident acoustic power and the power required to raise the tissue temperature by 1 °C (Supplementary Discussion 7), which were 0.62 for soft tissue thermal index and 0.38 for cranium thermal index. According to an official statement of the American Institute of Ultrasound in Medicine, for a thermal index less than or equal to 1.5, there is no time limit for adult transcranial ultrasound because any thermal exposure would be below thresholds for bioeffects (https://www.aium.org/resources/official-statements/view/recommended-maximum-scanning-times-for-displayed-thermal-index-(ti)-values).

Volumetric ultrafast imaging

The temporal window is the most widely used imaging window for TCD and has become the standard for cerebral artery assessment[1] (Supplementary Fig. 13). Through the temporal window, we can achieve ultrasound insonation of the terminal ICA (TICA), which delivers blood from the neck to the major arteries in the brain, as well as the ACA, MCA and PCA, which deliver blood to most of the four brain lobes (frontal, parietal, temporal and occipital).

The cerebral arteries can be mapped by ultrafast ultrasound data acquisition followed by subsequent volumetric image reconstruction (Methods). Compared with conventional volumetric Doppler imaging, this method substantially enhances the signal-to-noise ratio (Supplementary Fig. 14). The 256 elements are activated to emit five diverging waves at different insonation angles at a 3,000-Hz pulse repetition frequency (Fig. 2a). For all insonation angles, the backscattered raw radiofrequency signals are saved. During subsequent image reconstruction, beamforming and coherent compounding (Supplementary Discussion 8) are performed on the raw signals, which allows the backscattered signals from all insonation angles to be recombined (Fig. 2a). Because signals from different insonation angles produce images of the same target object but different artefacts, signal recombination causes constructive summation of the target object but destructive summation of artefacts, boosting the object to background contrast[22]. A spatiotemporal clutter filter (for example, singular value decomposition in this work) separates tissue motion signals from blood flow signals in the compounded data based on the difference in their spatiotemporal coherences[28] (Supplementary Discussion 9). Additional filters are used to suppress the noise and enhance the vascular structures[29–31]. Finally, the filtered data are used to reconstruct a volumetric power Doppler image (Fig. 2a). The diverging waves and the multi-angle compounding method provide a wide ultrasound field, which simultaneously insonates the bilateral ACA, MCA, PCA, and TICA, mapping a large vascular
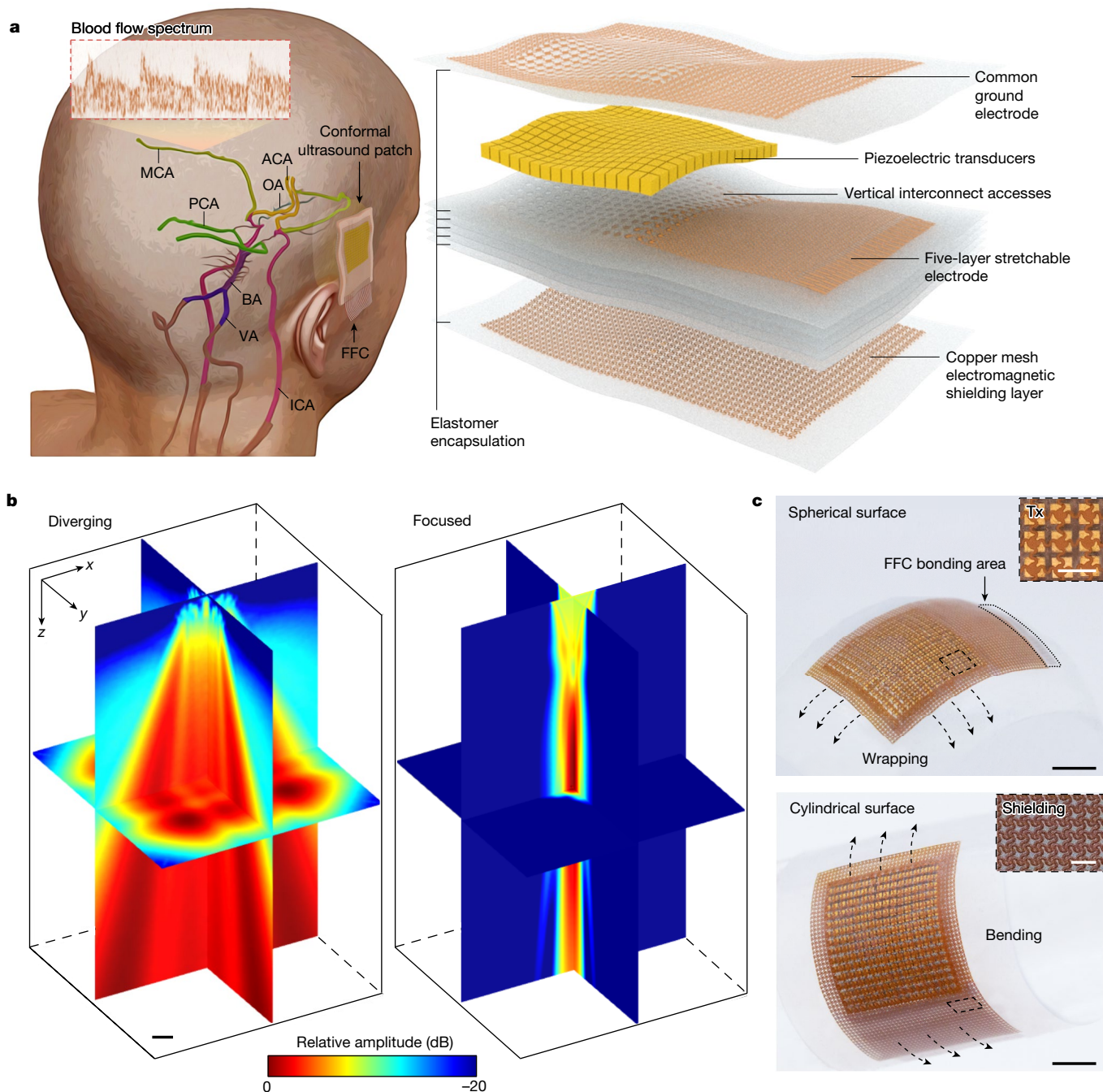
Fig. 1 | Overview of the conformal ultrasound patch for TCD. a, Schematic of the working configuration and patch structure. The patch is attached to the scalp for volumetric mapping of the major arteries in the brain[48]. Blood flow spectra of different target arteries are recorded. The patch consists of a 16 × 16 array of piezoelectric transducers connected by a five-layer stretchable electrode and a common ground electrode. A copper mesh is used as an electromagnetic shielding layer to enhance the signal-to-noise ratio. The entire device is encapsulated by a waterproof and biocompatible silicone elastomer. **b**, Simulation results of diverging and focused ultrasound fields based on 2D matrix array beamforming. The maximum derated spatial peak temporal average intensity of the focused ultrasound field is around 370 mW cm^{-2} for spectra monitoring, much below the threshold recommended by the Food and Drug Administration (720 mW cm^{-2}) (ref. 27). The simulation was performed using an open-source Matlab toolbox Field II. **c**, Optical images of the patch on a spherical surface and a cylindrical surface. The insets show the magnified transducer array (top) and the electromagnetic shielding layer (bottom). BA, basal artery; VA, vertebral arteries; OA, ophthalmic arteries; FFC, flat flexible cable; Tx, transducers. Scale bars, 5 mm (**b**,**c**); 1 mm (**c**, insets).

network (Fig. 2b for participant 1 and Supplementary Figs. 15–49 for participants 2–36).

We recorded volumetric power Doppler images during a carotid compression test and captured the flow variations in different arterial segments, which helped in identifying different cerebral arteries (Fig. 2c). Compressing the left common carotid artery mostly caused a decrease in flow in the left TICA and left MCA, a change in flow direction in the left ACA, an increase in flow in the left PCA and an increase in flow in most of the contralateral vessels (Supplementary Discussion 5). To semi-quantitatively evaluate the vascular network capacity, we evaluated the changes in the amplitude of the power Doppler signal of selected representative landmarks in each arterial segment. The results indicate that the collateral circulation could be recorded reliably (Fig. 2d and Extended Data Fig. 3).
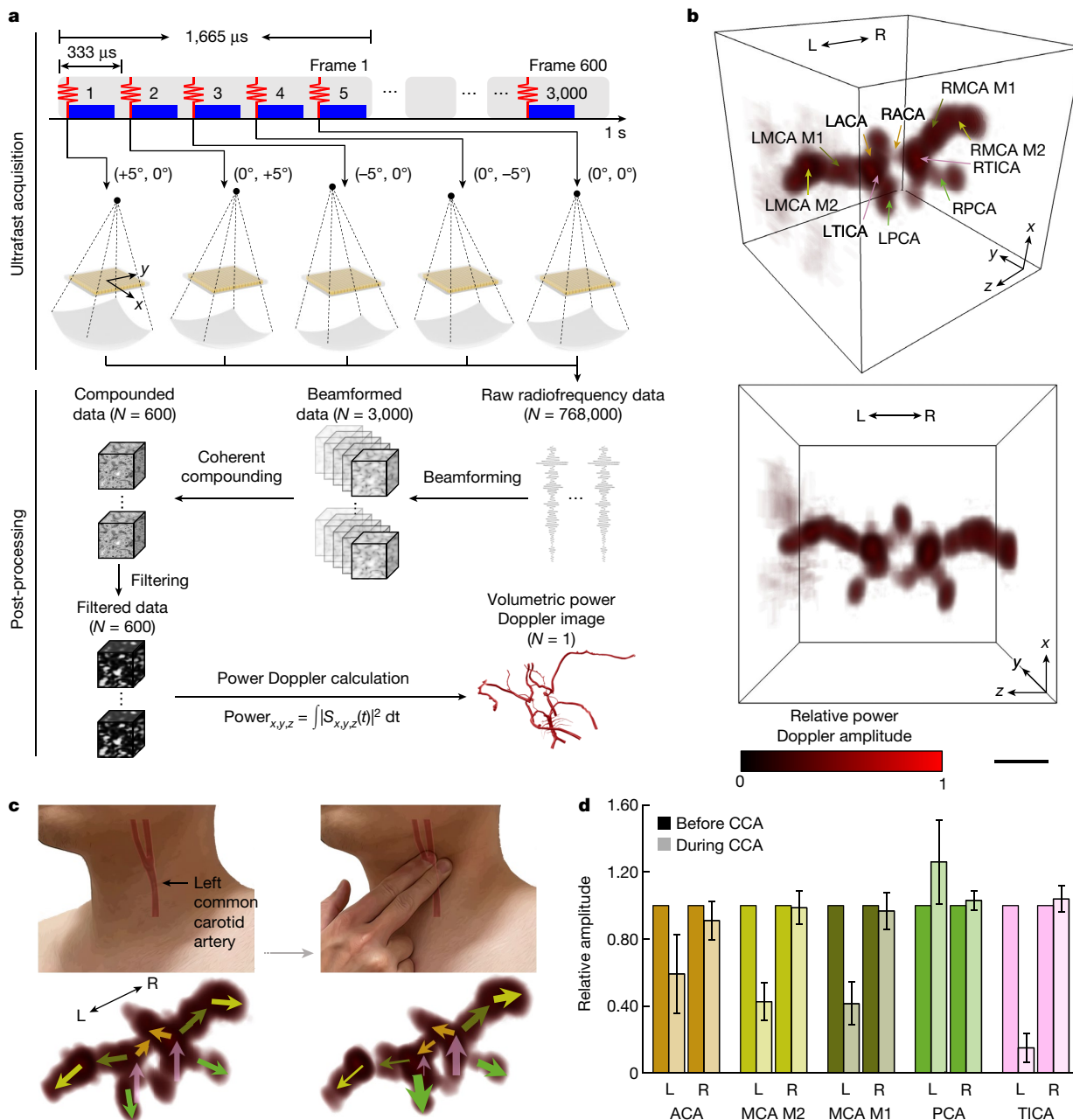
Fig. 2 | Volumetric ultrafast power Doppler imaging. a, Schematic of the imaging process. In ultrafast acquisition, five diverging waves with different insonation angles are quasi-simultaneously transmitted at a 3,000-Hz pulse repetition frequency. In post-processing, the acquired raw radiofrequency data go through beamforming, coherent compounding, singular value decomposition filtering and power Doppler calculation to reconstruct a volumetric power Doppler image. **b**, Different views of the volumetric power Doppler image of major cerebral arteries from participant 1 in a 60 × 60 × 60 mm³ region, acquired through the temporal window. Volumetric power Doppler images from participants 2–36 can be found in Supplementary Figs. 15–49. **c**, Comparison of volumetric power Doppler images before and during the left common carotid artery being compressed. The colour and thickness-coded arrows indicate the directions and magnitudes of blood flow in different arterial segments. **d**, Bar graph of compression carotid artery test. The power Doppler amplitudes of representative landmarks of bilateral arterial segments change accordingly before and during the compression of the left common carotid artery. The measurements were repeated three times on six participants. Error bars indicate 1 s.d. of the measurements. Note that individual anatomical variations, such as hypoplasia or aplasia of certain arteries, can affect these results[49]. The hypoplasia or aplasia arteries are observed in two of the six participants in this study. Each bar is colour-coded for different arterial segments (cider for ACA, xanthic for MCA M2, juniper for MCA M1, Kelly green for PCA and carnation pink for TICA). To better evaluate the relative change before and after compression, we normalized the results before compression and only considered the relative change of the blood flow during compression. L, left; R, right; CCA, compressing carotid artery. Scale bar, 10 mm (**b**).

Data processing and validation

Blood flow measurements by the conformal ultrasound patch were validated with a conventional TCD probe. We chose the circle of Willis as the model, which is composed of several major arteries that provide blood supply to the entire brain[1]. It has widespread branches, so the circle of Willis is usually measured through all four transcranial windows[24]. Each window targets different arterial segments (Supplementary Table 2): the temporal is best for the ACA, MCA M2, MCA M1, PCA and TICA; the orbital for the ophthalmic arteries and ICA siphon;
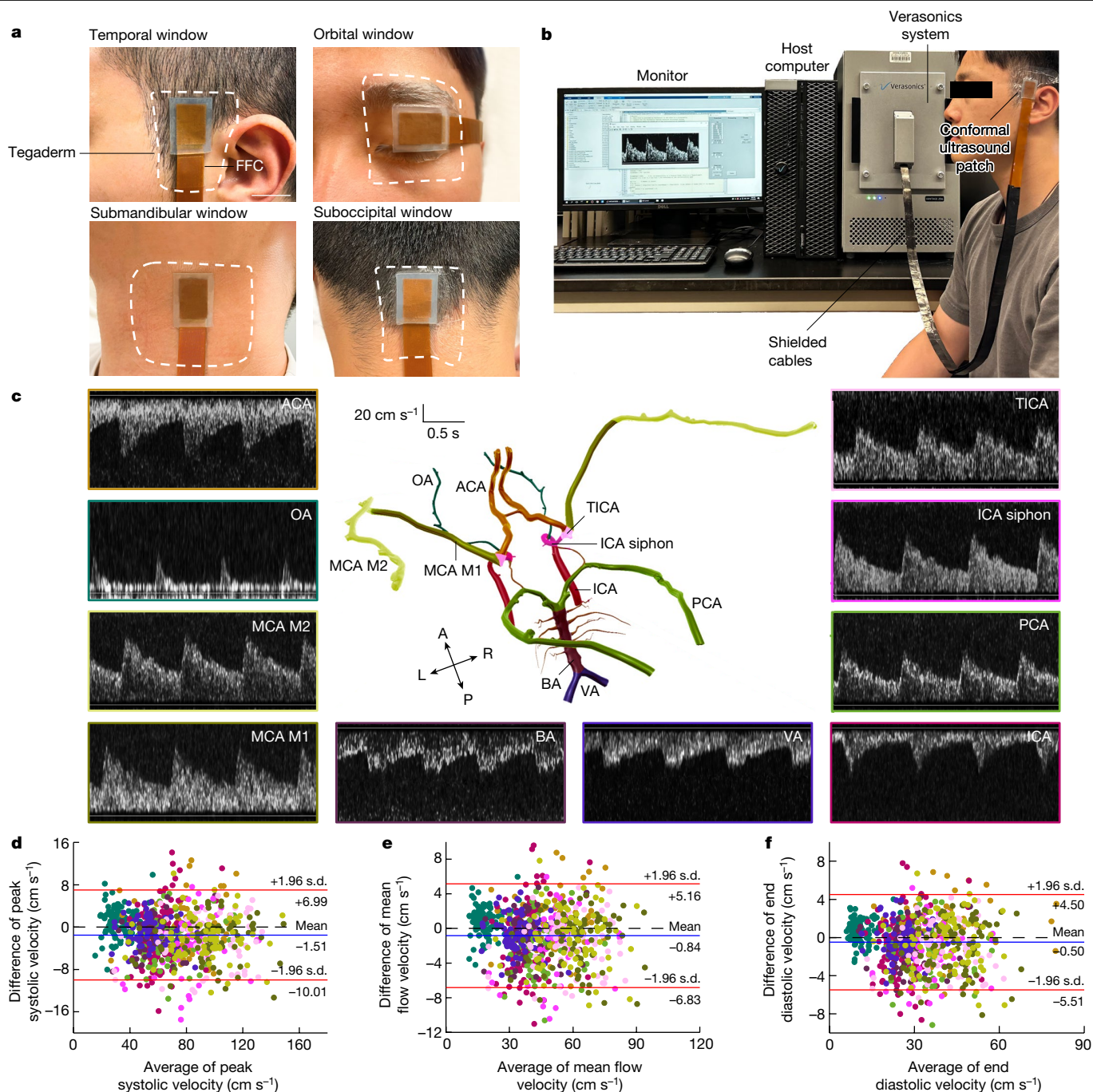
Fig. 3 | Validation of cerebral blood flow measurements. a, Optical images of the conformal ultrasound patch on four different transcranial windows, including the temporal, orbital, submandibular and suboccipital windows. **b**, Optical image of the complete setup. It includes the ultrasound patch connected to a Verasonics system by shielded (3304BC-S, 3 M) cables. The host computer controls the Verasonics system for data acquisition and processing. The blood flow spectrum is displayed on the monitor. **c**, Examples of blood flow spectra recorded from representative arterial segments from participant 1 by using the ultrasound patch. The spectra share the same scale bars. Blood flow spectra from participants 2–36 can be found in Supplementary Figs. 15–49. **d**–**f**, Bland–Altman plots of peak systolic velocity (**d**), mean flow velocity (**e**) and end diastolic velocity (**f**) measured by the ultrasound patch and a conventional TCD probe on 36 participants. Solid blue lines are the mean differences in the measurements between the two modalities. Solid red lines are 95% limits of agreement (that is, 1.96 s.d. above and below the mean differences), and black dash lines are the zero difference of the measurements between the two modalities. Each plot has 762 data points that are colour-coded for different arterial segments (that is, cider for ACA, dark cyan for ophthalmic arteries (OA), xanthic for MCA M2, juniper for MCA M1, boysenberry for basal artery (BA), blueberry for vertebral arteries (VA), hibiscus for ICA, Kelly green for PCA, magenta for ICA siphon and carnation pink for TICA). FFC, flat flexible cable; L, left; R, right; A, anterior; P, posterior. Scale bar, 2 cm (**a**).

the submandibular for the ICA; and the suboccipital for the basal artery and vertebral arteries (Fig. 3a). The setup consists of the conformal ultrasound patch linked to a commercial ultrasound machine (Vantage 256, Verasonics) with shielded cables for signal transmission, controlled by a host computer for data acquisition and processing (Fig. 3b).

We developed codes for Doppler processing to acquire high-resolution blood flow spectra (Fig. 3c for participant 1 and Supplementary Figs. 15–49 for participants 2–36) with functions such as automatic spectral envelope tracking, sample volume customization, and audio (Supplementary Discussion 10). The recorded spectra have

Table 1 | Demographics of participants

Characteristics	n (%) or mean ± s.d.
Sex	**n (%)**
Male	19 (52.8)
Female	17 (47.2)
Race or ethnicity	**n (%)**
White	15 (41.7)
Asian	13 (36.1)
Black or African	5 (13.9)
Hispanic or Latino	3 (8.3)
Underlying conditions	**n (%)**
Diabetes	5 (13.9)
Smoking	5 (13.9)
Cardiac disease	4 (11.1)
Obesity	3 (8.3)
Kidney disease	2 (5.6)
Cerebrovascular disease	1 (2.8)
Biometrics	**Mean ± s.d.**
Age (years)	52.92 ± 18.74
Height (cm)	167.44 ± 9.25
Weight (kg)	68.92 ± 11.72
Body mass index	24.46 ± 2.80

This table presents an overview of the demographic information for all participants in this study. Details include sex, race/ethnicity, underlying conditions, age, height, weight and body mass index, providing context for the diversity of the participants, which ensures that the findings of the study are broadly applicable.

a temporal resolution around 200 Hz, a velocity resolution of less than 0.01 cm s^{-1}, and a 128-colourmap of Doppler signal intensities, which are similar to the performance of the latest conventional TCD system (https://viasonix.com/products/transcranial-doppler/). This enables us to correlate variations in blood flow velocities to the corresponding cardiac phases (Supplementary Fig. 50). Spectral envelope tracking provides peak systolic velocity and end diastolic velocity, which enables the computation of mean flow velocity, pulsatility index and resistive index (Methods and Extended Data Fig. 4). Sample volume customization can provide blood flow distribution across the entire target arterial segment, which is valuable for identifying pathologic turbulent flow (Supplementary Discussion 11) in the low-velocity zone[2] (Supplementary Fig. 51). Real-time audio provides convenience for clinical training and diagnostics (Supplementary Video 1).

For this comparison study between the conformal ultrasound patch and a conventional TCD probe, we have collected blood flow velocities of 10 arterial segments from 36 adult volunteers for three times to ensure the results are reliable and reproducible (Table 1 and Methods). Intrinsically, a complete circle of Willis is observed in only about 30% of the population[32]. Moreover, participants with specific demographics and medical history tend to have abnormal cerebral arteries and may exhibit thicker, or even inaccessible, skull windows[24]. As a result, both the conventional probes and the ultrasound patch may encounter difficulties in detecting some or all cerebral arteries (Extended Data Table 2 and Supplementary Discussion 12).

Bland–Altman plots show that the mean differences and standard deviations (s.d.) of the differences between these two devices are −1.51 ± 4.34 cm s^{-1}, −0.84 ± 3.06 cm s^{-1}, −0.50 ± 2.55 cm s^{-1}, −0.0101 ± 0.0485, and −0.0040 ± 0.0186 for peak systolic velocity, mean flow velocity, end diastolic velocity, pulsatility index and resistive index, respectively (Fig. 3d–f, Supplementary Fig. 52 and Supplementary Discussion 13). These biases are much smaller than these metrics per se, indicating good agreement between these two devices. To delve deeper into our results, we apply scatter plots for a more thorough analysis (Supplementary Figs. 52 and 53). Notably, the squared correlation coefficients for all velocity parameters and indices exceed 0.9. This strong correlation underscores the consistency in the readings between these two devices.

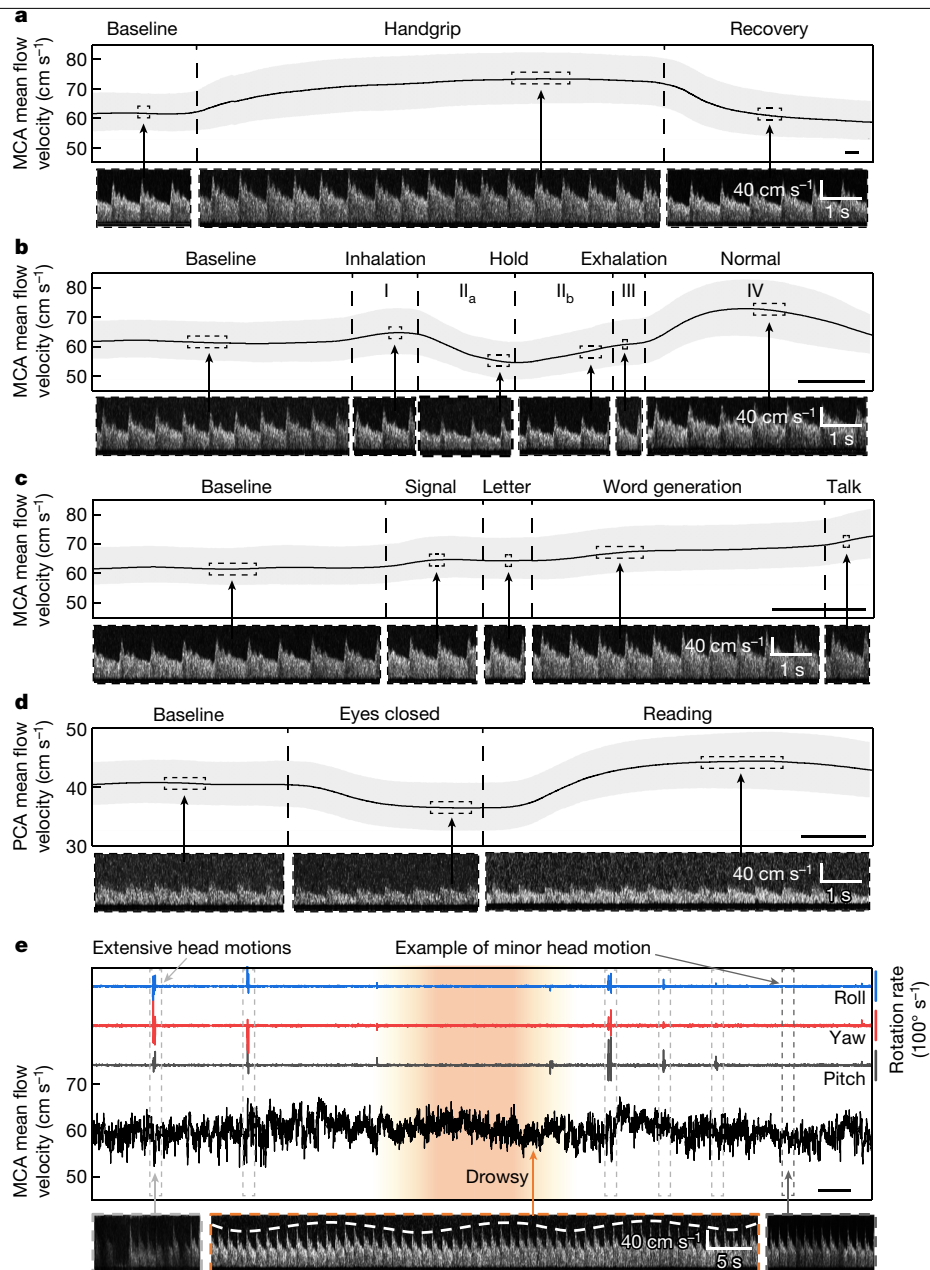## Monitoring under different scenarios

The brain can regulate its blood flow to meet physiological demands (Supplementary Discussion 14). Surveillance of these regulations can be used to evaluate neurological functions. The conformal ultrasound patch was used to measure (using the temporal window) MCA and PCA flows, which dominate the supply of blood to the brain. The motion tolerance of the device was determined to be within about ±20° with head roll, yaw and pitch (Supplementary Fig. 54). Rotating the head beyond this range may shift the alignment between the ultrasound beam and arteries, resulting in signal degradation or loss. We then asked the participants to conduct four different activities that modulated haemodynamics in specific cerebral arteries (Methods and Supplementary Fig. 55). Each activity was repeated 15 times to minimize interference of confounding factors.

The handgrip involves the contraction of the forearm muscles that activate the sympathetic nervous system, leading to an increase in blood supply to the brain and therefore the contralateral MCA blood flow velocity[33]. The test consists of three phases: resting baseline, right handgrip and recovery. The left MCA mean flow velocity rose rapidly at the beginning of the handgrip, then slowly plateaued at around 119% baseline velocity when the handgrip was maintained. The flow velocity decreased swiftly to 95% baseline velocity immediately after the handgrip was released and gradually reached a plateau towards the end of the recovery phase (Fig. 4a).

The Valsalva manoeuvre provides an estimate of the autoregulatory capacity[34]. It changes the intrathoracic pressure, which affects the venous return, cardiac output, blood pressure and, therefore, cerebral blood flow. We monitored the left MCA mean flow velocity during four sequential phases. In phase I, the participants inhaled deeply; the intrathoracic pressure increased, which led to a decrease in the heart rate and a slight (about 5%) increase in the cerebral blood flow. In phase IIa, the participants held their breath; the venous return decreased, which led to a decrease in the heart rate and around 12% drop in the blood flow. In phase IIb, the baroreflex was activated, which increased the heart rate and partially restored the blood flow. In phase III, the participants exhaled; blood was refilled to the pulmonary vasculature, leading to an increase in the heart rate and slight variations (an increase in most participants) in the blood flow. Finally, in phase IV, the participants resumed normal breathing; the venous return increased, resulting in a decrease in the heart rate and subsequent overshoot (about 118%) of the cerebral blood flow. Once the venous return went back to normal, the blood flow dropped back to the baseline (Fig. 4b).

Word generation is commonly used in functional TCD to understand language processing and production. In this activity, a cue tone was used for auditory signal stimulation, and then a letter was given to the participants. The participants were asked to use the letter to generate words and orally report them after a second auditory signal stimulation. The recorded left MCA mean flow velocity showed a rise (approximately 5%) from the baseline on hearing the tone and after a letter was provided. Activation of the language centre of the brain led to an increased demand for cerebral blood flow in the dominant hemisphere[35]. The velocity remained at an average of about 110% baseline during word generation and continued to increase (by about 18%) when the participant was reporting the words (Fig. 4c).

Visual stimulation can change the blood flow in the visual cortex[36]. We monitored the PCA that supplies blood to the primary vision centre in the brain (that is, the occipital lobe) when the participants

Fig. 4 | Monitoring of cerebral haemodynamics under different scenarios.
a–**d**, Mean blood flow velocities of target arteries recorded during different
activities (handgrip (**a**), Valsalva manoeuvre (**b**), word generation (**c**) and visual
stimulation (**d**)). The measurements for each activity were repeated 15 times on
six participants. Solid black lines are the average results and grey regions denote
±1 s.d. The corresponding spectra are snapshots showing representative flow
characteristics in each phase of the activity. The blood flow spectra share the
same scale bars. **e**, The mean flow velocity in the MCA and the corresponding
gyroscope data during a continuous 4-h recording. Rotation rates of rolling,
yawing and pitching are denoted by blue, red and black lines, respectively.
Transient signal loss periods due to extensive head motions and a spectrum
during this period are labelled with light-grey dashed boxes. An example of
minor head motion and a spectrum during this period are labelled with dark-grey
dashed boxes. The participant felt drowsy at around 2 h into the recording. The
figure labelled with an orange dashed box highlights the flow characteristics
during this period. Intracranial B waves with a frequency of about three cycles
in 1 min are labelled by a white dashed line. The blood flow spectra share the
same scale bars. Scale bars, 5 s (**a**–**d**); 10 min (**e**).

closed their eyes and then opened their eyes to read. The left PCA
mean flow velocity decreased to around 90% baseline with eyes closed
and gradually increased until it peaked (around 110% baseline) with
reading (Fig. 4d).

These transient cerebral haemodynamic changes are the result of
the activities of the participants and can be impaired or inhibited if
pathological conditions exist[37]. The recorded cerebral blood flow pro-
files during these activities follow similar trends as those measured by
conventional TCD probes[33–36], indicating a potential clinical benefit
for monitoring cerebral haemodynamics using the conformal patch.

Because it allows hands-free, wearable measurements, the confor-
mal ultrasound patch is particularly useful for prolonged surveillance
(Extended Data Fig. 5). For example, intracranial B waves during sleep
are closely related to the glymphatic system activities, which is impor-
tant for toxic waste by-product removal in the brain and disease recov-
ery[38,39] (Supplementary Discussion 15). These events are accompanied
by slow, spontaneous oscillations in the cerebral blood flow velocity
(that is, B waves) at 0.3–4 cycles per minute[40]. With the conformal ultra-
sound patch at the temporal window, we monitored the cerebral blood
flow spectra in the MCA in a participant for 4 h continuously (Fig. 4e).

The recording has a high signal-to-noise ratio, except for transient signal fluctuations during extensive head motions (Fig. 4e and Supplementary Fig. 56). Minor head motions, which the participant naturally made, does not significantly affect the signal quality (Fig. 4e). A cascade of B waves was identified when the participant felt drowsy (Fig. 4e). Prolonged surveillance is also valuable for cerebral emboli monitoring and therefore embolic stroke prevention. Evidence suggests that extending the recording time can capture more patients positive for an embolic signal[10]. The conformal ultrasound patch could detect flowing emboli in a phantom (Supplementary Fig. 57), demonstrating the promise of prolonged recording using the conformal patch in a clinical setting.

Discussion

TCD is a powerful ultrasound modality for neurovascular diagnostics and research, but the conventional form factor limits continuous measurements of cerebral arteries and can only image 1D or 2D planes of the complex 3D network. To develop a conformal ultrasound patch for continuous TCD application, we have designed a soft 2D matrix array for volumetric imaging and electronically locating target arterial segments from the complex 3D cerebral arterial network. The conformal ultrasound patch coupled with ultrafast signal acquisition enables volumetric imaging of the cerebral arterial network and simplifies the blood flow data acquisition process from target vessels. Using the reconstructed volumetric image, we can electronically focus the low-intensity ultrasound beam to acquire cerebral blood flow measurements from various segments of the 3D arterial network. The design notably minimizes operator dependency and enhance motion tolerance in comparison to conventional TCD probes (Supplementary Discussion 16). Moreover, a comprehensive survey of feedback from all participants indicated that a majority (69.4%) prefer the conformal ultrasound patch for its comfort (Supplementary Fig. 58). With these advantages, we demonstrate not only blood flow measurements from different segments of the major cerebral arteries and transcranial monitoring of cerebral haemodynamics under different scenarios (for example, carotid compression test, handgrip, Valsalva manoeuvre, word generation and visual stimulation) but also long-term monitoring during drowsiness with minimal signal loss. These results have notable implications for both clinical diagnostic tools for brain disorders and medical research on neurovascular functions (Supplementary Discussion 16).

The synergy between the conformal ultrasound patch and ultrafast volumetric reconstruction enables haemodynamics monitoring in complex 3D vascular networks. Therefore, apart from cerebral arteries, this technology can also be used to study the complex haemodynamics in other clinically important vessels, such as the carotid bifurcation. The structural morphology of these arteries induces turbulent blood flow, prone to atherosclerosis and emboli generation[41]. The conformal ultrasound patch can detect both gas and solid emboli (Supplementary Fig. 57), potentially enabling early detection for timely intervention before severe pathological progression in major arteries.

This study primarily focuses on the development of the front-end ultrasound patch, the related ultrafast imaging algorithms and the validation of their applications in transcranial volumetric imaging and cerebral blood flow monitoring. With future development, the performance of the device and functionality could be further enhanced.

First, the conformal ultrasound patch has limited spatial resolution. Signals from major cerebral arteries can be obtained, but the patch neglects information from arterioles, venules and capillaries. Obtaining signals from all vessels can provide a more holistic insight into the cerebrovascular system. Thus, to improve the spatial resolution, contrast agents such as microbubbles[42] may be needed to generate much higher amplitude echoes compared with the surrounding tissues (Supplementary Discussion 17). Ultrafast ultrasound localization microscopy can potentially be adopted to overcome the diffraction limit, enabling super-resolution transcranial imaging and full reconstruction of deep vascular systems down to the level of capillaries[43,44]. Furthermore, by using harmonic imaging, the incident ultrasound waves can drive the microbubbles to vibrate nonlinearly, generating strong harmonic components in echoes[45] (Supplementary Discussion 18). Moreover, time reversal can be used to calculate precise time delays on each element of the transducer array and thus partially compensate for the phase aberration of the skull[46].

Second, the volumetric image reconstruction was post-processed subsequently after data acquisition. This post-processing time may hinder the workflow of the clinicians when needing to dynamically target different segments of the cerebral arterial network in real time. Improvement in volumetric reconstruction speed can be realized by a multi-threaded process with much higher computational power for image reconstruction. The calculation and image rendering processes could be highly parallelized and optimized for real-time imaging[47], which may be valuable for understanding the real-time functional connectivity of the brain.

Third, the conformal ultrasound patch was connected to the Verasonics system for all data acquisition processes. Volumetric imaging requires a relatively high-power supply to successfully transmit and receive ultrasound waves through the transcranial windows into the deep brain. Moreover, the ultrafast data acquisition process and long-term measurements of blood flow velocity can generate a large dataset (for example, 1–5 GB), which requires a powerful system for fast data transfer and processing. Back-end systems based on customized printed circuit boards or application-specific integrated circuits can significantly miniaturize the control system with reduced power consumption to provide higher freedom of movement for long-term wearability[16] (Supplementary Discussion 19).

Fourth, transient signal fluctuations were observed in the long-term recording due to ultrasound beam misalignment to the target during extensive head motions. Machine-learning algorithms can be used to identify signal loss, automatically track the targeted arterial segment, eliminate occasions of signal loss and improve reliability in clinical utility during continuous measurements.

Finally, all participants in this study were healthy without severe neurological pathologies related to cerebral haemodynamics. Further testing across large populations, including particularly those patients with neurovascular conditions, such as vasospasm, stenoses, aneurysms and embolism, can potentially enable diagnostic parameters for the early detection of major neurological pathologies.

Online content

Any methods, additional references, Nature Portfolio reporting summaries, source data, extended data, supplementary information, acknowledgements, peer review information; details of author contributions and competing interests; and statements of data and code availability are available at https://doi.org/10.1038/s41586-024-07381-5.

1. Aaslid, R. (ed.) *Transcranial Doppler Sonography* (Springer Science+Business Media, 2012).
2. Alexandrov, A. V. et al. Practice standards for transcranial Doppler (TCD) ultrasound. Part II. Clinical indications and expected outcomes. *J. Neuroimaging* **22**, 215–224 (2012).
3. Lohmann, H., Ringelstein, E. B. & Knecht, S. in *Handbook on Neurovascular Ultrasound* Vol. 21 (ed. Baumgartner, R. W.) 251–260 (Karger, 2006).
4. Gambhir, S. S. Molecular imaging of cancer with positron emission tomography. *Nat. Rev. Cancer* **2**, 683–693 (2002).
5. Withers, P. J. et al. X-ray computed tomography. *Nat. Rev. Methods Primers* **1**, 18 (2021).
6. Weiskopf, N., Edwards, L. J., Helms, G., Mohammadi, S. & Kirilina, E. Quantitative magnetic resonance imaging of brain anatomy and in vivo histology. *Nat. Rev. Phys.* **3**, 570–588 (2021).
7. Seubert, C. N., Cibula, J. E. & Mahla, M. E. in *Textbook of Neurointensive Care* (eds Layon, A. J. et al.) 109–126 (Springer, 2013).
8. Tidswell, T., Gibson, A., Bayford, R. H. & Holder, D. S. Three-dimensional electrical impedance tomography of human brain activity. *NeuroImage* **13**, 283–294 (2001).
9. Fantini, S., Sassaroli, A., Tgavalekos, K. T. & Kornbluth, J. Cerebral blood flow and autoregulation: current measurement techniques and prospects for noninvasive optical methods. *Neurophotonics* **3**, 031411 (2016).

Article

10. Mackinnon, A. D., Aaslid, R. & Markus, H. S. Long-term ambulatory monitoring for cerebral emboli using transcranial Doppler ultrasound. *Stroke* **35**, 73–78 (2004).
11. Ivancevich, N. M. et al. Real-time 3-D contrast-enhanced transcranial ultrasound and aberration correction. *Ultrasound Med. Biol.* **34**, 1387–1395 (2008).
12. Pietrangelo, S. J., Lee, H.-S. & Sodini, C. G. A wearable transcranial Doppler ultrasound phased array system. In *Proc. Intracranial Pressure & Neuromonitoring XVI* Vol. 126 (Heldt, T.) 111–114 (Springer, 2018).
13. Lin, M., Hu, H., Zhou, S. & Xu, S. Soft wearable devices for deep-tissue sensing. *Nat. Rev. Mater.* **7**, 850–869 (2022).
14. Wang, C. et al. Bioadhesive ultrasound for long-term continuous imaging of diverse organs. *Science* **377**, 517–523 (2022).
15. Hu, H. et al. Stretchable ultrasonic arrays for the three-dimensional mapping of the modulus of deep tissue. *Nat. Biomed. Eng.* **7**, 1321–1334 (2023).
16. Lin, M. et al. A fully integrated wearable ultrasound system to monitor deep tissues in moving subjects. *Nat. Biotechnol.* **42**, 448–457 (2023).
17. Zhang, L. et al. A conformable phased-array ultrasound patch for bladder volume monitoring. *Nat. Electron.* **7**, 77–90 (2024).
18. Wang, C. et al. Monitoring of the central blood pressure waveform via a conformal ultrasonic device. *Nat. Biomed. Eng.* **2**, 687–695 (2018).
19. Hu, H. et al. A wearable cardiac ultrasound imager. *Nature* **613**, 667–675 (2023).
20. Gao, X. et al. A photoacoustic patch for three-dimensional imaging of hemoglobin and core temperature. *Nat. Commun.* **13**, 7757 (2022).
21. Kyriakou, A. et al. A review of numerical and experimental compensation techniques for skull-induced phase aberrations in transcranial focused ultrasound. *Int. J. Hyperthermia.* **30**, 36–46 (2014).
22. Montaldo, G. et al. Ultrafast compound Doppler imaging: a new approach of Doppler flow analysis. In *Proc. 2010 IEEE International Symposium on Biomedical Imaging: From Nano to Macro* 324–327 (IEEE, 2010).
23. Bercoff, J. et al. Ultrafast compound Doppler imaging: providing full blood flow characterization. *IEEE Trans. Ultrason. Ferroelectr. Freq. Control* **58**, 134–147 (2011).
24. Alexandrov, A. V. et al. Practice standards for transcranial Doppler ultrasound: part I—test performance. *J. Neuroimaging* **17**, 11–18 (2007).
25. Smith, S. W. et al. The ultrasound brain helmet: feasibility study of multiple simultaneous 3D scans of cerebral vasculature. *Ultrasound Med. Biol.* **35**, 329–338 (2009).
26. Lindsey, B. D. et al. The ultrasound brain helmet: new transducers and volume registration for in vivo simultaneous multi-transducer 3-D transcranial imaging. *IEEE Trans. Ultrason. Ferroelectr. Freq. Control* **58**, 1189–1202 (2011).
27. Food and Drug Administration. *Marketing Clearance of Diagnostic Ultrasound Systems and Transducers: Guidance for Industry and Food and Drug Administration Staff.* Report No. FDA-2017-D-5372 (Food and Drug Administration, 2023).
28. Demené, C. et al. Spatiotemporal clutter filtering of ultrafast ultrasound data highly increases Doppler and fultrasound sensitivity. *IEEE Trans. Med. Imaging* **34**, 2271–2285 (2015).
29. Jerman, T., Pernus, F., Likar, B. & Spiclin, Z. Enhancement of vascular structures in 3D and 2D angiographic images. *IEEE Trans. Med. Imaging* **35**, 2107–2118 (2016).
30. Huang, C. et al. Debiasing-based noise suppression for ultrafast ultrasound microvessel imaging. *IEEE Trans. Ultrason. Ferroelectr. Freq. Control* **66**, 1281–1291 (2019).
31. Fan, L., Zhang, F., Fan, H. & Zhang, C. Brief review of image denoising techniques. *Vis. Comput. Ind. Biomed. Art* **2**, 7 (2019).
32. Jones, J. D., Castanho, P., Bazira, P. & Sanders, K. Anatomical variations of the circle of Willis and their prevalence, with a focus on the posterior communicating artery: a literature review and meta-analysis. *Clin. Anat.* **34**, 978–990 (2021).
33. Nogueira, R. C. et al. Dynamic cerebral autoregulation changes during sub-maximal handgrip maneuver. *PLoS One* **8**, e70821 (2013).
34. Tiecks, F. P. et al. Effects of the Valsalva maneuver on cerebral circulation in healthy adults: a transcranial Doppler study. *Stroke* **26**, 1386–1392 (1995).
35. Knecht, S., Henningsen, H., Deppe, M. & Huber, T. Successive activation of both cerebral hemispheres during cued word generation. *Neuroreport* **7**, 820–824 (1996).
36. Olah, L. et al. Visually evoked cerebral vasomotor response in smoking and nonsmoking young adults, investigated by functional transcranial Doppler. *Nicotine Tob. Res.* **10**, 353–358 (2008).
37. Silverman, A. & Petersen, N. *Physiology, Cerebral Autoregulation* (StatPearls, 2022).
38. Fultz, N. E. et al. Coupled electrophysiological, hemodynamic, and cerebrospinal fluid oscillations in human sleep. *Science* **366**, 628–631 (2019).
39. Newell, D. W., Nedergaard, M. & Aaslid, R. Physiological mechanisms and significance of intracranial B waves. *Front. Neurol.* **13**, 872701 (2022).
40. Newell, D. W., Aaslid, R., Stooss, R. & Reulen, H. J. The relationship of blood flow velocity fluctuations to intracranial pressure B waves. *J. Neurosurg.* **76**, 415–421 (1992).
41. Gildenberg, P. L., O'Brien, R. P., Britt, W. J. & Frost, E. A. The efficacy of Doppler monitoring for the detection of venous air embolism. *J. Neurosurg.* **54**, 75–78 (1981).
42. Chong, W. K., Papadopoulou, V. & Dayton, P. A. Imaging with ultrasound contrast agents: current status and future. *Abdom. Radiol.* **43**, 762–772 (2018).
43. Demene, C. et al. Transcranial ultrafast ultrasound localization microscopy of brain vasculature in patients. *Nat. Biomed. Eng.* **5**, 219–228 (2021).
44. Renaudin, N. et al. Functional ultrasound localization microscopy reveals brain-wide neurovascular activity on a microscopic scale. *Nat. Methods* **19**, 1004–1012 (2022).
45. Anvari, A., Forsberg, F. & Samir, A. E. A primer on the physical principles of tissue harmonic imaging. *Radiographics* **35**, 1955–1964 (2015).
46. Fink, M. Time reversal of ultrasonic fields. I. Basic principles. *IEEE Trans. Ultrason. Ferroelectr. Freq. Control* **39**, 555–566 (1992).
47. Rabut, C. et al. 4D functional ultrasound imaging of whole-brain activity in rodents. *Nat. Methods* **16**, 994–997 (2019).
48. Human Anatomy Atlas 2024 v.2024.00.005 (Visible Body, 2024).
49. Makowicz, G., Poniatowska, R. & Lusawa, M. Variants of cerebral arteries - anterior circulation. *Pol. J. Radiol.* **78**, 42–47 (2013).

Methods

Device fabrication

Electrode design and patterning. The electrode is composed of a common ground electrode, a five-layer stretchable electrode and a copper mesh electromagnetic shielding layer. First, polyimide (poly(pyromellitic dianhydride-*co*-4,4′-oxydianiline) amic acid solution, PI2545 precursor, HD MicroSystems) was spin-coated on copper sheets (Oak-Mitsui) at 4,000 rpm for 60 s, followed by soft baking on a hotplate at 100 °C for 3 min and subsequently at 150 °C for 1 min, and then hard baking in a nitrogen oven at 300 °C for 1 h, yielding a 2-μm thick polyimide layer coated on 20 μm thick copper sheets.

Polydimethylsiloxane (Sylgard 184 silicone elastomer) was then spin-coated at 3,000 rpm for 60 s on a glass slide and cured in an 80 °C oven as a temporary substrate for electrode transfer. To improve bonding, the polyimide-coated copper sheets and the polydimethylsiloxane-coated glass slides were activated by ultraviolet light (PSD series Digital UV Ozone System, Novascan) for 3 min.

The polyimide-coated side of the copper sheet was then attached to the polydimethylsiloxane-coated glass slide. The bilayer copper/polyimide film was laser ablated (Laser Mark's, central wavelength, 1,059–1,065 nm; power, 0.228 mJ; frequency, 35 kHz; speed, 300 mm s⁻¹; and pulse width, 500 ns) following electrode patterns designed with AutoCAD (Autodesk) (Supplementary Fig. 7).

Electronic packaging. On two separate glass slides, polymethyl methacrylate (495PMMA, Kayaku Advanced Materials), serving as a sacrificial layer, was spin-coated at 2,000 rpm for 60 s and cured at 80 °C for 30 min. Then, a 12-μm thick silicone (Ecoflex-0030, Smooth-On) was spin-coated at 4,000 rpm for 60 s and cured at room temperature for 2 h.

To assemble the device, a water-soluble tape (5414 Transparent, 3 M) was used for transfer printing the ground electrode to an Ecoflex-coated glass slide and the copper mesh electromagnetic shielding layer to another Ecoflex-coated glass slide. The water-soluble tape was then removed by immersing it in 80 °C water for 30 min. Conductive epoxy (Von Roll 3022 E-Solder, EIS) was placed on the 256 bonding pads of the island-bridge layout of the common ground electrode. After that, the matrix array of 1–3 composites (Del Piezo Specialties) was bonded to the bonding pads by curing a conductive epoxy for 8 h at room temperature and then 2 h at 40 °C to avoid high-temperature-induced depolarization of the 1–3 composites.

On the glass slide with the copper mesh electromagnetic shielding layer, sequential transfer printing of the five-layer stretchable electrode was done, and it was stacked one on top of another by water-soluble tape. Each layer was bonded to a flat flexible cable (Premo-Flex FPC Jumper, Molex) using solder paste ($Sn_{42}Bi_{57.6}Ag_{0.4}$ (melting point, 138 °C)) and spin-coated with a 25-μm thick Ecoflex layer at 2,200 rpm for 60 s and cured at room temperature for 2 h. Laser ablation was used to create vertical interconnect accesses through the Ecoflex layers to expose the 256 bonding pads in the five-layer stretchable electrode[50]. Then, this glass slide was bonded to the 1–3 composite on the other glass slide using conductive epoxy followed by curing.

Finally, the gaps between the two glass slides were filled with Ecoflex followed by curing at room temperature. The glass slides were removed by dissolving the polymethyl methacrylate in acetone to release the conformal ultrasound patch.

Acoustic field simulation

We simulated the diverging and focused ultrasound beams using an open-source Matlab toolbox Field II. The medium was set as uniform with a sound speed of 1,540 m s⁻¹ and a density of 1,000 kg m⁻³. The centre frequency was set to 2 MHz, the same as that of the real probe. We applied the built-in function, 'xdc_2d_array', to create the transducer array. The transmission time delay of each transducer element could be individually set to emit a diverging beam or a focused beam.

Device performance characterizations

A network analyser (Hewlett-Packard 4195 A) was used to measure the electrical impedance and phase angle of each transducer in the device (Supplementary Fig. 8). Based on the electrical impedance graph, the resonant frequency (f_r), the frequency with the lowest electrical impedance, and anti-resonant frequency (f_a), the frequency with the highest electrical impedance, of the transducers were mapped (Supplementary Fig. 8). The effective electromechanical coupling coefficient (k_{eff}) was calculated by

$$k_{eff} = \sqrt{1 - \frac{f_r^2}{f_a^2}} \qquad (1)$$

The pulse-echo response and bandwidth of the device were characterized (Supplementary Fig. 8). An aluminium block was placed 8 cm away from the device in a water tank. The back-end system (Vantage 256, Verasonics) was used to obtain raw radiofrequency signals by transmitting and receiving ultrasound pulse waves. Fast Fourier transform in Matlab R2021a was used to transfer the signals into the frequency domain.

Crosstalk between adjacent transducer elements was characterized by changing the transmitting frequencies and activation voltages (Supplementary Fig. 8). A sinusoidal peak-to-peak voltage of 15 V was applied by a functional generator (3390, Keithley) to excite one of the elements with different frequencies from 1 MHz to 3 MHz. Moreover, we used a 2-MHz transmission with activation voltages from 5 V to 25 V. The reference voltages received by adjacent elements were measured. Then, the crosstalk was calculated by

$$\text{Crosstalk} = 20 \log \left(\frac{\text{Reference voltage of the adjacent element}}{\text{Activation voltage of the excited element}} \right) \quad (2)$$

The signal-to-noise ratio with and without the copper mesh electromagnetic shielding layer was tested with a 1-mm thick thread underwater (Supplementary Fig. 8).

Safety-measurement procedures

To evaluate the safety of the device, the acoustic exposure was evaluated using a 3D ultrasound mapping system (AIMS III hydrophone scanning system, ONDA) following the provided calibration procedures. We used a calibrated hydrophone (Model HNP-0400, ONDA) to scan the ultrasound field in 3D in a water tank (Extended Data Fig. 2). The hydrophone was connected to an oscilloscope (PicoScope 5244A, ONDA), and software (Soniq v.5.3.1.0, ONDA) was used to control the scanning. We scanned a zone of $60 \times 60 \times 100$ mm³ below the device with a spatial resolution of 0.1 mm with and without a formalin-fixed temporal bone specimen (about 5 mm in thickness, desiccated, with skin, fascia and marrow removed, provided by the Medical Education and Anatomical Services at the University of California San Diego). The acoustic intensity was controlled by changing the activation voltage. We calculated safety indices (spatial peak pulse average intensity, spatial peak temporal average intensity, mechanical index and thermal indices) and compared them with the maximum levels recommended by the Food and Drug Administration[27].

Volumetric ultrafast power Doppler imaging

The protocol consisted of two steps: ultrafast signal acquisition and post-processing. For signal acquisition, we used different time-delay profiles to transmit the diverging waves from five virtual sources that were 22.30 mm behind the device to obtain a view angle of 40° (Fig. 2a). We used three cycles of tone burst centred at 2 MHz with a

pulse repetition frequency of 3,000 Hz to activate the transducers. A group of five diverging waves was transmitted and received repeatedly 600 times within 1 s (Fig. 2a). The digitization rate of the received analog signals was 7.8125 MHz.

For post-processing, volumetric beamforming was performed on the raw radiofrequency data from each transducer 3,000 times. The beamformed data with different diverging waves were coherently compounded to form 600 frames of images. We implemented spatiotemporal clutter filtering (for example, singular value decomposition in this work) to separate blood flow (incoherent motion within the volume) from tissue motion (coherent motion within the volume) (Supplementary Discussion 9). After filtering, the energy of the temporal signal was integrated over the whole imaging block to calculate the power Doppler intensity in 3D (Fig. 2a). The computational load is inversely proportional to the size of each reconstructing voxel in the target region. We used a $0.77 \times 0.77 \times 0.77$ mm^3 voxel, which corresponds to one wavelength of the ultrasound at 2 MHz in soft tissues, to maintain adequate spatial resolution and reasonable computational load.

To characterize the performance of this protocol, we conducted a test by using a Doppler flow phantom (ATS 523A, CIRS). We pumped Doppler fluid (769DF, CIRS) through the phantom with an internal diameter of 4 mm, positioned at an approximate depth of 60–80 mm. The volumetric flow imaging result (Supplementary Fig. 59) shows the flow profile of the phantom and is highly consistent with the ground truth collected by a conventional TCD probe (P4_2v, Verasonics).

Volumetric imaging by diverging waves is data and computation intensive. The raw radiofrequency data obtained within 1 s were approximately 800 MB. On beamforming and coherent compounding, the in-phase and quadrature data were inflated to approximately 4 GB. Subsequent processing steps, including singular value decomposition filtering, effectively reduced the final volumetric result to a more manageable size of around 5 MB. The data processing was executed within 10 min using a MacBook Pro equipped with an M1 Max chip, a 32-core graphical processing unit, and 64 GB of unified memory.

Automatic tracking of blood flow envelope

We first applied histogram equalization to enhance the contrast between the blood flow spectra and background noise, which improved the accuracy of envelope tracking (Extended Data Fig. 4). After that, we defined a step function to fit the spectra at each moment, which had a value of 1 in the frequency band lower than f_{step} (the envelope to be extracted), and 0 in the frequency band higher than f_{step} (Extended Data Fig. 4). The sum of the absolute differences at all frequencies between the spectra and the step function was defined as the error to quantify the fitting. We swept the frequency f_{step} from the lower (0 Hz) to the higher frequency (2,850 Hz) boundaries of the spectra and obtained the corresponding error values (Extended Data Fig. 4). The f_{step} value corresponding to the smallest error was the extracted envelope at this moment (Extended Data Fig. 4).

Study design for device validation

This study compared the cerebral blood flow measurements from the conformal ultrasound patch and a conventional TCD probe (P4_2v, Verasonics) to validate the agreement and correlation of their measurements at multiple arterial segments (that is, ACA, MCA M2, MCA M1, PCA, ophthalmic arteries, ICA, ICA siphon, TICA, basal artery and vertebral arteries). All studies on human participants in this work were approved by the Institutional Review Board at the University of California, San Diego (IRB #805201). The study was registered on ClinicalTrials.gov (NCT06073145). The inclusion criteria specified that the participants must be older than 18 years and in generally good health, without any severe medical conditions. The eligibility for the study was determined through a conversational screening process. Thirty-six participants in a random series were recruited and informed

of the potential risks and experimental procedures. Written consent forms were obtained before the test. The results had a statistical power of 83.07% to detect a difference of 5 cm s^{-1} on blood flow velocities, assuming a s.d. of 10 cm s^{-1} using a paired t-test with a 0.05 two-sided significance level. This statistical power is larger than the general statistical power requirement (that is, 80%) for clinical trials[51,52].

S. Zhou conducted all measurements throughout the study. We have taken several steps to ensure the accuracy and reliability of the measurements. First, S. Zhou completed online courses from The Institute for Advanced Medical Education about TCD (https://www.iame.com/online-courses/vascular/transcranial-doppler-TCD-CME) before conducting the tests. Second, this student received several hands-on training sessions from A. Lam, a clinically qualified ultrasonographer with more than 30 years of experience in TCD, before performing the measurements. Third, the student strictly adhered to the guidance[24,53] to ensure the accuracy of the measurements during the testing process. Finally, D.W. Newell, another clinically qualified TCD ultrasonographer, provided guidance and supervision during the testing process and reviewed the results after the measurements, further ensuring the accuracy and reliability of the reference measurements. To illustrate the validity of the measurements made by S. Zhou, we compared the blood flow spectra obtained from A. Lam and S. Zhou by using a conventional TCD probe (Supplementary Fig. 60).

All procedures were conducted in accordance with the TCD examination guidelines[24,53]. The participants were instructed to sit comfortably in a chair. The soft ultrasound patch and conventional rigid TCD probe were performed randomly in sequence for each participant. The ultrasound patch or a conventional TCD probe was placed on the temporal, orbital, submandibular and suboccipital windows to monitor different arterial segments. The temporal window can be further divided into anterior, middle and posterior windows[1] (Supplementary Fig. 13). The temporal window that provided the best cerebral signal in the TCD examination was selected for each participant.

The procedure for adhering the patch to the skin was as follows. First, we applied a layer of ultrasound gel to the surface of the target area. Next, we positioned the patch on the designated testing spot, ensuring the even distribution of the gel without any overflow onto the device surface. Finally, we secured the patch on the testing spot using Tegaderm (1626W, 3 M). This method ensured a stable adhesion between the patch and the skin, allowing for robust data acquisition. Diverging waves were used to reconstruct the volumetric power Doppler image, which facilitated the identification of various cerebral arteries. We then used focused waves to continuously monitor the blood flow spectra at target arterial segments.

We used a fast 3 s sweep speed that allowed a detailed examination of the spectra. A higher pulse repetition frequency led to higher measurement limits of Doppler shift (that is, a wider range of blood flow velocities) and also increased the ultrasound energy exposure. To balance the measurement limits and safety concerns, we chose a pulse repetition frequency of 2,500–4,000 Hz. The zero Doppler shift line (that is, baseline) was placed near the top or bottom of the screen to avoid aliasing (Supplementary Fig. 61). In the case of weak velocity signals, we increased the gain with a slow sweeping speed to visualize the Doppler shifts in the spectra. We lowered the power output of the devices, with a derated spatial peak temporal average intensity of $I_{SPTA.3} < 17$ mW cm^{-2} (Food and Drug Administration Track 1 maximum recommended value for ophthalmic scans) to insonate through the orbital window to reduce ultrasound exposure of the eye[27].

Adhering to the ALARA (as low as reasonably achievable) principle[27] for general ultrasound diagnosis, we reduced the mechanical index and thermal index to limit the ultrasound exposure level during monitoring (Extended Data Fig. 6).

After identifying and optimizing the spectra of each arterial segment, we continued the recordings for 30 s. The time interval for switching between the patch and the TCD probe was approximately

5 min. In our study design, we anticipated generating 360 comparative sets of blood flow spectral measurements from 36 participants. However, owing to anatomical variations, some arterial segments were inaccessible, resulting in the acquisition of 254 comparative datasets. For each dataset, we conducted three repeated measurements, yielding a total of 762 individual data points for analysis. We calculated the average of peak systolic velocity, mean flow velocity, end diastolic velocity, pulsatility index and resistive index based on the recorded spectra for those 254 arterial segments. The measurements were concluded once 30 s spectral data of all arterial segments were recorded by both modalities three times. Data agreement was evaluated by Bland–Altman analysis (Fig. 3d–f and Supplementary Fig. 52). Data correlation was evaluated by scatter plots (Supplementary Figs. 52 and 53). No adverse events were reported throughout the duration of the examination.

Protocol for monitoring cerebral haemodynamics

To establish the baseline, the participants sat comfortably in a chair. The conformal ultrasound patch was attached to the temporal window. Flow spectra were monitored with focused beams on target arterial segments.

Hand grip. The protocol consisted of 40 s of resting, followed by 3 min of handgrip and subsequently 80 s of recovery (Supplementary Fig. 55). During the handgrip, the participants held a handgrip exerciser and exerted 30% of their maximum contraction force continuously. Switching of the test phases was signalled with cue tones.

Valsalva manoeuvre. The protocol started with a 20-s baseline recording. Following this, the participants inhaled deeply for 5 s (phase I), held their breath for 15 s (phases IIa and IIb), exhaled fully for 2.5 s (phase III) and finally breathed normally (phase IV) (Supplementary Fig. 55).

Word generation. After 15 s of baseline recording, the participants were first signalled by a cue tone for 3 s, given a letter visually for 2.5 s after a 2-s rest, and then asked to silently generate as many words as possible starting with this letter within 15 s and to orally report the words within 2.5 s (Supplementary Fig. 55).

Visual stimulation. A news magazine with emotionally neutral text was used. The protocol consisted of 20 s of baseline recording, 20 s of eye closing and 40 s of eye opening and reading silently (Supplementary Fig. 55). Changes between phases were signalled with cue tones.

To minimize the interference of confounding factors, each activity was performed 15 times on six participants. The interval between each test was more than 10 min or until the recorded values had returned to the baseline. The mean flow velocity was obtained from the recorded spectra and was expressed as mean ± s.d.

Long-term monitoring. The participant was instructed to lie supine on a bed and remain as still as possible throughout the monitoring session. This positioning ensured that the patch was not in direct contact with the pillow and that the head was not pressing on the patch. The ultrasound patch was securely affixed to the participant's temporal window by Tegaderm (1626W, 3 M) for volumetric imaging. The MCA position was then located and targeted by a focused ultrasound beam. We placed a wearable gyroscope in close proximity to the ultrasound patch. This enabled us to correlate head movements with any changes in signal quality. The recording was conducted without interruption for 4 h until the device was powered off.

Data availability

The data in this study are available at Figshare (https://doi.org/10.6084/m9.figshare.25448254.v1)[54].

Code availability

The code used in this study is available at GitHub (https://github.com/Yup0626/TCD).

50. Huang, Z. et al. Three-dimensional integrated stretchable electronics. *Nat. Electron.* **1**, 473–480 (2018).
51. Julious, S. A. Sample sizes for clinical trials with normal data. *Stat. Med.* **23**, 1921–1986 (2004).
52. Julious, S. A. *Sample Sizes for Clinical Trials* (CRC Press, 2023).
53. American Institute of Ultrasound in Medicine. The AIUM practice parameter for the performance of the musculoskeletal ultrasound examination. *J. Ultrasound Med.* E23–E35 (2023).
54. Zhou, S. Shared data for "Transcranial volumetric imaging using a conformal ultrasound patch". figshare https://doi.org/10.6084/m9.figshare.25448254.v1 (2024).
55. Moehring, M. A. & Spencer, M. P. Power M-mode Doppler (PMD) for observing cerebral blood flow and tracking emboli. *Ultrasound Med. Biol.* **28**, 49–57 (2002).
56. Muehllehner, G. & Karp, J. S. Positron emission tomography. *Phys. Med. Biol.* **51**, R117 (2006).
57. Høedt-Rasmussen, K., Sveinsdottir, E. & Lassen, N. A. Regional Cerebral low in Man Determined by Intra-arterial Injection of Radioactive Inert Gas. *Circ. Res.* **18**, 237–247 (1966).
58. Yandrapalli, S. & Puckett, Y. *SPECT Imaging*. (StatPearls Publishing, 2020).
59. Pindzola, R. R. & Yonas, H. The xenon-enhanced computed tomography cerebral blood flow method. *Neurosurgery* **43**, 1488–1491 (1998).
60. Hoeffner, E. G. et al. Cerebral perfusion CT: technique and clinical applications. *Radiology* **231**, 632–644 (2004).
61. Shaban, S. et al. Digital subtraction angiography in cerebrovascular disease: current practice and perspectives on diagnosis, acute treatment and prognosis. *Acta Neurol. Belg.* **122**, 763–780 (2022).
62. Boxerman, J. L. et al. Consensus recommendations for a dynamic susceptibility contrast MRI protocol for use in high-grade gliomas. *Neuro-oncology* **22**, 1262–1275 (2020).
63. Petcharunpaisan, S., Ramalho, J. & Castillo, M. Arterial spin labeling in neuroimaging. *World J. Radiol* **2**, 384–398 (2010).
64. Kety, S. S. & Schmidt, C. F. The determination of cerebral blood flow in man by the use of nitrous oxide in low concentrations. *Am. J. Physiol.* **143**, 53–66 (1945).
65. Wilson, E. M. & Halsey, J. H. Jr Bilateral jugular venous blood flow by thermal dilution. *Stroke* **1**, 348–355 (1970).
66. Carter, L. P. Thermal diffusion flowmetry. *Neurosurg. Clin. N. Am.* **7**, 749–754 (1996).
67. Bagshaw, A. P. et al. Electrical impedance tomography of human brain function using reconstruction algorithms based on the finite element method. *NeuroImage* **20**, 752–764 (2003).
68. Le Roux, P. in *Textbook of Neurointensive Care*, 127–145 (Springer, 2013).
69. Samaei, S. et al. Time-domain diffuse correlation spectroscopy (TD-DCS) for noninvasive, depth-dependent blood flow quantification in human tissue in vivo. *Sci. Rep.* **11**, 1–10 (2021).
70. Moerman, A. & Wouters, P. Near-infrared spectroscopy (NIRS) monitoring in contemporary anesthesia and critical care. *Acta Anaesthesiol. Belg.* **61**, 185–194 (2010).
71. Sanderson, M. & Yeung, H. Guidelines for the use of ultrasonic non-invasive metering techniques. *Flow Meas* **13**, 125–142 (2002).
72. Willie, C. K. et al. Utility of transcranial Doppler ultrasound for the integrative assessment of cerebrovascular function. *J. Neurosci. Methods* **196**, 221–237 (2011).
73. Bakker, S. L. et al. Cerebral haemodynamics in the elderly: the rotterdam study. *Neuroepidemiology* **23**, 178–184 (2004).
74. Brunser, A. M. et al. Transcranial Doppler in a Hispanic-Mestizo population with neurological diseases: a study of sonographic window and its determinants. *Brain Behav* **2**, 231–236 (2012).
75. Wong, K. S. et al. Use of transcranial Doppler ultrasound to predict outcome in patients with intracranial large-artery occlusive disease. *Stroke* **31**, 2641–2647 (2000).
76. Marinoni, M., Ginanneschi, A., Forleo, P. & Amaducci, L. Technical limits in transcranial Doppler recording: Inadequate acoustic windows. *Ultrasound Med. Biol.* **23**, 1275–1277 (1997).
77. Itoh, T. et al. Rate of successful recording of blood flow signals in the middle cerebral artery using transcranial Doppler sonography. *Stroke* **24**, 1192–1195 (1993).
78. Chan, M. Y. et al. Success Rate of Transcranial Doppler Scanning of Cerebral Arteries at Different Transtemporal Windows in Healthy Elderly Individuals. *Ultrasound Med. Biol.* **49**, 588–598 (2023).
79. Lee, C. H., Jeon, S. H., Wang, S. J., Shin, B. S. & Kang, H. G. Factors associated with temporal window failure in transcranial Doppler sonography. *Neurol. Sci.* **41**, 3293–3299 (2020).
80. Lin, Y.-P., Fu, M.-H. & Tan, T.-Y. Factors Associated with No or Insufficient Temporal Bone Window Using Transcranial Color-coded Sonography. *J. Med. Ultrasound* **23**, 129–132 (2015).
81. Bazan, R. et al. Evaluation of the Temporal Acoustic Window for Transcranial Doppler in a Multi-Ethnic Population in Brazil. *Ultrasound Med. Biol.* **41**, 2131–2134 (2015).
82. Yagita, Y. et al. Effect of transcranial Doppler intensity on successful recording in Japanese patients. *Ultrasound Med. Biol.* **22**, 701–705 (1996).
83. Wijnhoud, A. D., Franckena, M., van der Lugt, A., Koudstaal, P. J. & Dippel, E. D. Inadequate acoustical temporal bone window in patients with a transient ischemic attack or minor stroke: role of skull thickness and bone density. *Ultrasound Med. Biol.* **34**, 923–929 (2008).
84. Nader, J. A., Andrade, M. L., Espinosa, V., Zambrano, M. & Del Brutto, O. H. Technical difficulties due to poor acoustic insonation during transcranial Doppler recordings in Amerindians and individuals of European origin. A comparative study. *Eur. Neurol.* **73**, 230–232 (2015).

Article

85. Kwon, J. H., Kim, J. S., Kang, D. W., Bae, K. S. & Kwon, S. U. The thickness and texture of temporal bone in brain CT predict acoustic window failure of transcranial Doppler. *J. Neuroimaging* **16**, 347–352 (2006).

86. Krejza, J. et al. Suitability of temporal bone acoustic window: conventional TCD versus transcranial color-coded duplex sonography. *J. Neuroimaging* **17**, 311–314 (2007).

Author contributions S.Z. and S.X. conceived the project. S.Z., X.G., G.P., X.Y. and B.Q. performed the experiments. S.Z. and X.G. performed the data processing and simulations. S.Z. and G.P. analysed the data. S.Z., G.P., X.G. and S.X. wrote the paper. All authors provided constructive and valuable feedback on the Article.
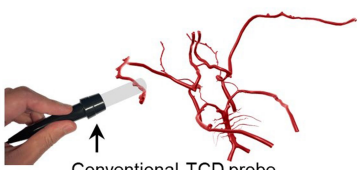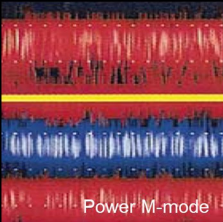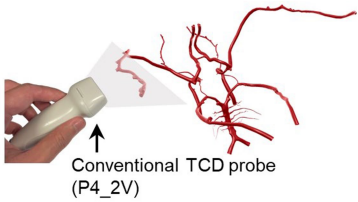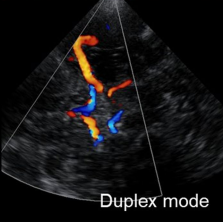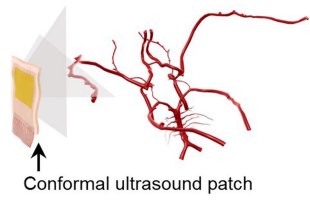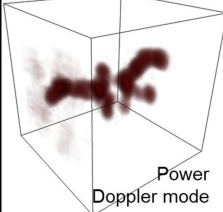
TCD sonography	Schematics	Results
1D	Conventional TCD probe (Multigon® TOC1M)	Power M-mode
2D	Conventional TCD probe (P4_2V)	Duplex mode
3D	Conformal ultrasound patch	Power Doppler mode

Extended Data Fig. 1 | 1D, 2D, and 3D TCD sonography. TCD sonography can be performed in different modes. The conventional TCD probe with a single transducer insonates target arteries in 1D, and the power M-mode results show collected blood flow signals[55]. The conventional phased array probe with a linear transducer array insonates target arteries in two dimensions. The acquired duplex mode (that is, combined B-mode and color Doppler mode) results show the collected tissue signals and blood flow directions in the plane (https://www.medison.ru/ultrasound/gal641.htm). The conformal ultrasound patch with a matrix array insonates the target arteries in 3D, and the power

Doppler mode results show the collected volumetric blood flow signals. A much larger computation power will be needed to reconstruct volumetric duplex mode images. Because we only consider the morphology of the vasculature rather than the surrounding tissues and blood flow directions, we focus on the power Doppler mode in this study. Note that conventional probes require handholding, which is impractical for long-term monitoring and generates results that are operator-dependent. The conformal ultrasound patch is self-adherent and overcomes these two challenges.
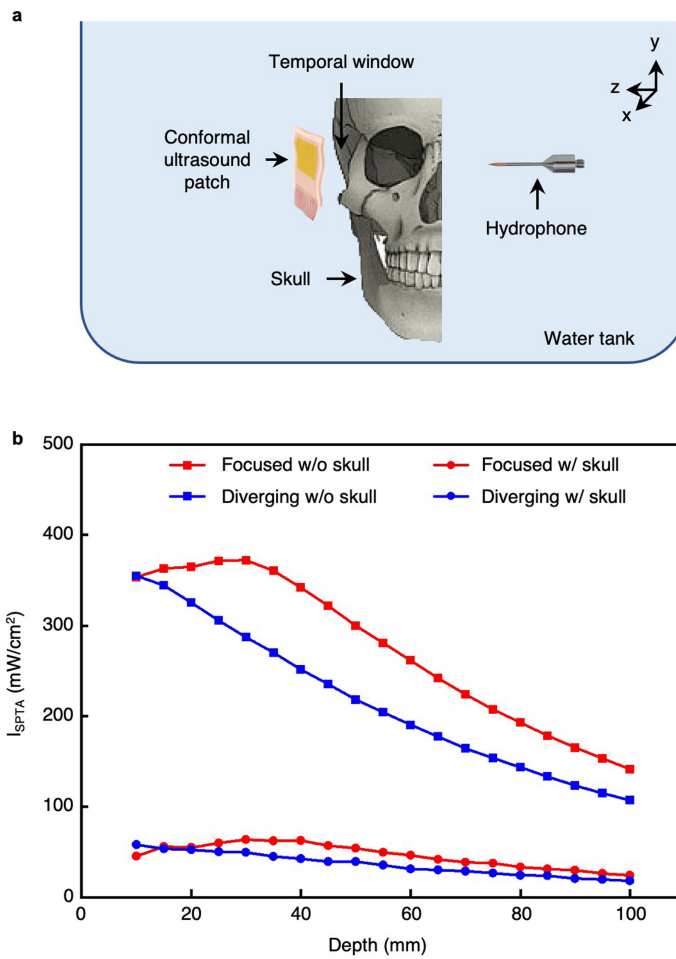
Extended Data Fig. 2 | Ultrasound exposure safety. a, System set-up for characterizing ultrasound exposure safety. The hydrophone is controlled by a 3D linear motor in a water tank. A formalin-fixed human skull sample is used to evaluate skull induced attenuation. **b**, Ultrasound intensity measured by the hydrophone. The maximum derated intensities of both diverging and focused beamforming strategies before derating are set to around 370 mW cm^{-2}. The average intensity loss of the ultrasound beams after skull penetration is around 83% for both beamforming strategies. All of the measured results are lower than the maximum level recommended by the Food and Drug Administration (that is, 720 mW cm^{-2})[27].
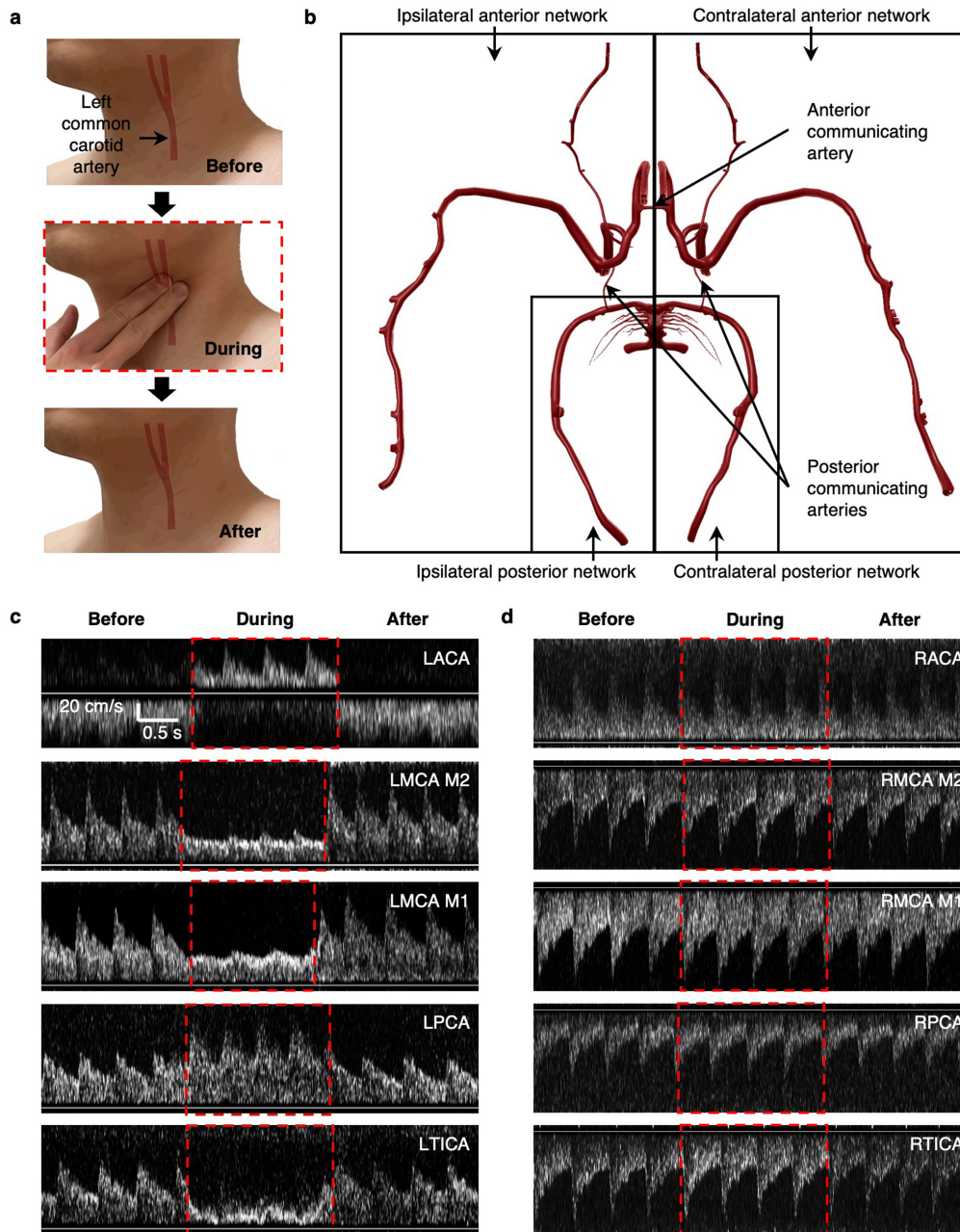
Extended Data Fig. 3 | Blood flow spectra of compressing the left common carotid artery. a, Schematics of before, during, and after the compression test. **b**, The circle of Willis can be divided into four parts, including ipsilateral anterior, contralateral anterior, ipsilateral posterior, and contralateral posterior networks. These four parts are connected by one anterior communicating artery and two posterior communicating arteries[48]. **c**, The blood flow spectra of ACA, MCA M2, MCA M1, PCA, and TICA segments on the left side before, during, and after the compression test. The red dashed boxes label the period during the compression. **d**, The blood flow spectra of ACA, MCA M2, MCA M1, PCA, and TICA segments on the right side before, during, and after the compression test. The red dashed boxes label the period during the compression. The spectra share the same scale bars.
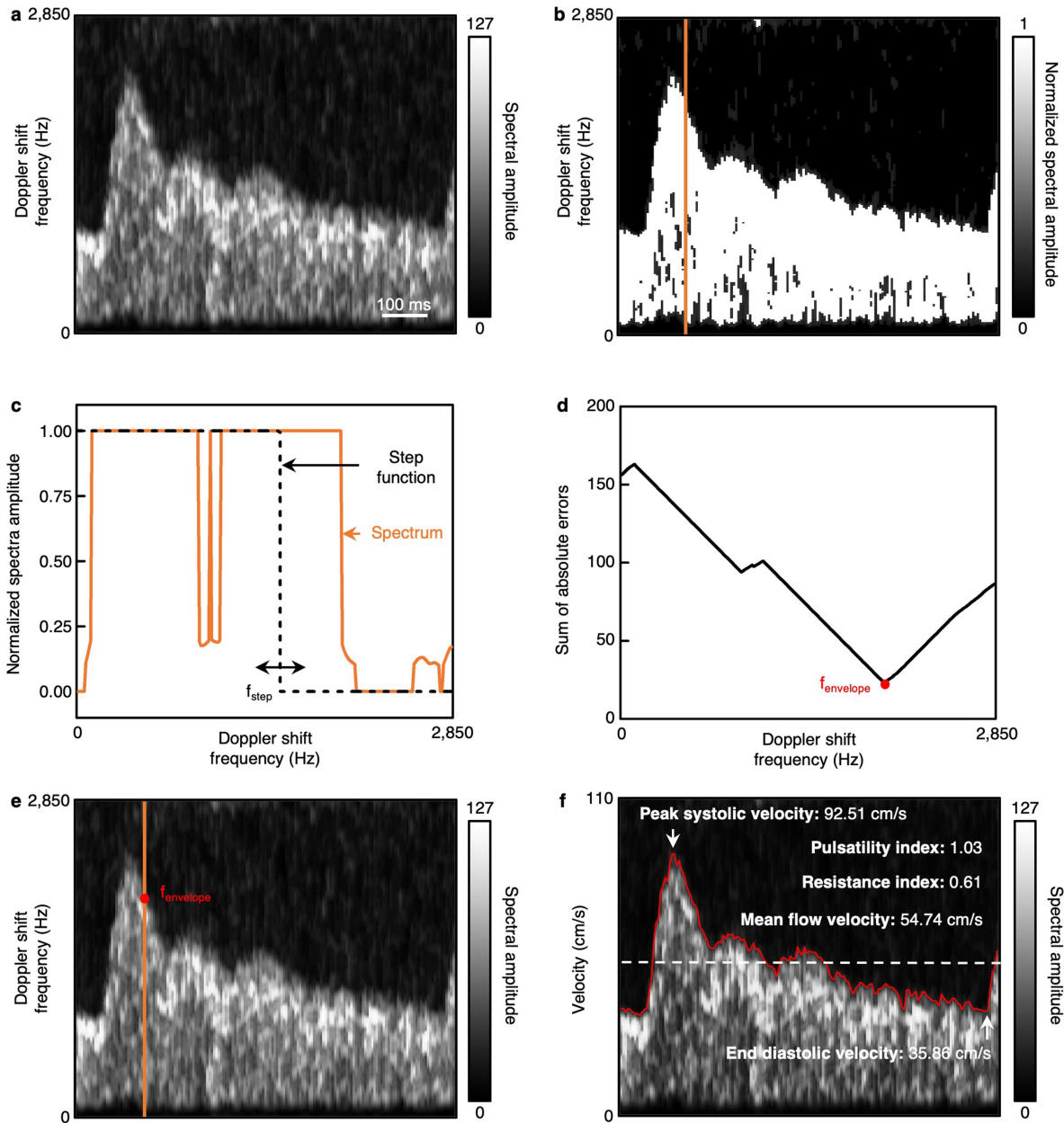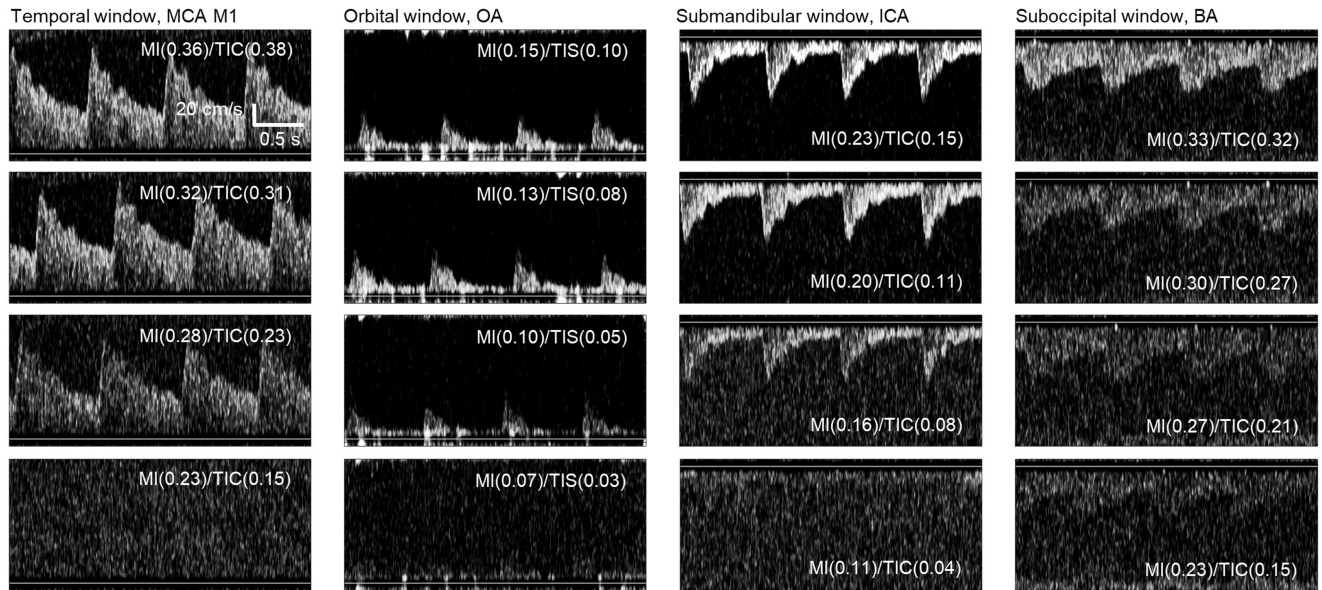
Extended Data Fig. 4 | Autonomous envelope tracking and parameter calculation. a, Spectrum Doppler of blood flow in one cardiac cycle. **b**, The spectrum Doppler is normalized first. After that, the spectrum with an amplitude higher than 0.2 is set 1, while the spectrum with an amplitude lower than 0.1 is set 0. This enhances the contrast between spectrum Doppler and noise. **c**, The orange curve is the amplitude snapshot of the enhanced spectrum in **b**, as labelled by the orange line. The enhanced spectrum has a similar shape like a step function. Therefore, we fit the spectrum using a step function to extract the envelope. The dashed black curve is one example of a step function.

Changing f_{step} will form different step functions. **d**, To find the step function that fits the spectrum the best, the sum of absolute errors is defined to quantify the difference between the spectrum curve and the step function. f_{step} sweeps from 0 to 2,850 Hz. The f_{step} corresponding to the minimum sum of absolute errors is the desired $f_{envelope}$. **e**, $f_{envelope}$ is the envelope corresponding to the spectrum at one moment. **f**, The entire envelope is extracted using the above method and labelled by a red line. The peak systolic velocity, mean flow velocity, end diastolic velocity, pulsatility index, and resistance index are calculated based on the tracked envelope. The spectra share the same timescale bar.

Extended Data Fig. 5 | Optical images of using different devices for TCD sonography. a, Optical images of a participant during and after using the conventional TCD probe for 30 min. The pressing results in discomfort and redness patterns on the skin. **b**, Optical images of the participant during and after using a conventional TCD headset for 30 min. The screwing and pressing result in discomfort and redness patterns on the skin. **c**, Optical images of the participant during and after using a customized TCD headset for 30 min. This headset is designed for monitoring cerebral blood flow during brain procedures. The screwing and pressing result in discomfort and redness patterns on the skin. **d**, Optical images of the participant during and after using the conformal ultrasound patch for 30 min. This mechanical design eliminates the need for uncomfortable pressure and substantially reduces skin irritation. The images share the same scale bar. The inset images share the same scale bar.

Temporal window, MCA M1

MI(0.36)/TIC(0.38)

20 cm/s

0.5 s

MI(0.32)/TIC(0.31)

MI(0.28)/TIC(0.23)

MI(0.23)/TIC(0.15)

Orbital window, OA

MI(0.15)/TIS(0.10)

MI(0.13)/TIS(0.08)

MI(0.10)/TIS(0.05)

MI(0.07)/TIS(0.03)

Submandibular window, ICA

MI(0.23)/TIC(0.15)

MI(0.20)/TIC(0.11)

MI(0.16)/TIC(0.08)

MI(0.11)/TIC(0.04)

Suboccipital window, BA

MI(0.33)/TIC(0.32)

MI(0.30)/TIC(0.27)

MI(0.27)/TIC(0.21)

MI(0.23)/TIC(0.15)

Extended Data Fig. 6 | Doppler spectra acquired from all transcranial windows by using different mechanical indices and thermal indices. As the mechanical index and thermal index decrease, the signal quality correspondingly declines. The optimal mechanical indices and thermal indices were chosen to be as low as reasonably achievable during blood flow monitoring, balancing safety and signal quality. For the temporal and suboccipital windows, the optimal mechanical index and thermal index were around 0.3; for the orbital window, we selected mechanical index around 0.13 and thermal index around 0.08; and for the submandibular window, the ideal mechanical index and thermal index were approximately 0.2 and 0.11, respectively. Importantly, these thresholds could be subject to individual variations due to physiological and anatomical differences. The spectra share the same scale bars. MI, mechanical index. TIC, cranium thermal index. TIS, soft tissue thermal index.

Extended Data Table 1 | Comparison of different techniques for cerebral blood flow monitoring

Method	Techniques	Invasiveness	Continuous	Absolute / Relative	Wearable	References
Nuclear medicine	Positron emission tomography	Yes	No	Absolute	No	[56]
	Intra-arterial injection of ^{133}Xe and [85]Kr	Yes	No	Absolute	No	[57]
	Single-photon emission computed tomography	Yes	No	Relative	No	[58]
X-ray	Xe-enhanced computed tomography	No	No	Absolute	No	[59]
	Perfusion computed tomography	Yes	No	Absolute	No	[60]
	Digital subtraction angiography	Yes	No	Absolute	No	[61]
Magnetic resonance imaging	Dynamic susceptibility contrast magnetic resonance imaging	Yes	No	Absolute	No	[62]
	Arterial spin labeling	No	Yes	Absolute	No	[63]
Intravascular measurements	Nitrous oxide inhalation	Yes	No	Absolute	No	[64]
Thermal probes	Jugular thermodilution	Yes	No	Absolute	No	[65]
	Thermal diffusion flowmetry	Yes	Yes	Absolute	Yes	[66]
Electrical probes	Electrical impedance tomography	No	Yes	Relative	Yes	[8,67]
	Electroencephalography	No	Yes	Relative	Yes	[7]
Optical probes	Laser Doppler flowmetry	Yes	Yes	Absolute	Yes	[68]
	Diffuse correlation spectroscopy	No	Yes	Relative	Yes	[69]
	Near-infrared spectroscopy	No	Yes	Absolute	Yes	[70]
Ultrasonography	Transit-time ultrasound flowmetry	Yes	Yes	Absolute	No	[71]
	Transcranial Doppler	No	Yes	Absolute	Yes	[72]

Invasiveness, continuous monitoring, absolute or relative quantification, and wearability of the different techniques are compared. These parameters allow for analysing the advantages and disadvantages of current techniques to guide the design of the conformal ultrasound patch. References 7,8,56–72.

Article

Extended Data Table 2 | Exemplary large group studies on TCD success rates

Number of Participants	Sex (Female percentage)	Acoustic Intensity (mW/cm^2)	Age (mean ± standard deviation) (years)	Race / Ethnicity	Success Rate (percentage)	Reference
2,735	56.7%	N/A	71.5±6.6	N/A	75% (A; D)	[73]
749	52.2%	N/A	<60 (n = 375); 60-79 (n = 230); ≥80 (n = 144)	Hispanic–Mestizo	94.9%; 70.4%; 56.3% (O; D)	[74]
705	41.8%	N/A	67.7±11.9	Mostly Asian	75% (A; D)	[75]
624	39.7%	550	55.2±16.1	N/A	92.8% (O; N/A)	[76]
597	24.5%	100	<40 (n = 43); 40-69 (n = 384); ≥70 (n = 170)	Mostly Asian	77.1% (N/A; D)	[77]
396	64.7%	N/A	62.6±6.0	Mostly Asian	72.2% (A; D)	[78]
376	35.9%	N/A	68.4±12.1	Asian	83.5% (A; D)	[79]
355	38.6%	N/A	64.5±13.2	Mostly Asian	71.2% (O; D)	[80]
262	48.9%	N/A	66±N/A	White (n = 202); Black or African American/Asian (n = 60)	79.8% (A; D)	[81]
239	46.9%	532; 456; 380; 304; 228; 152; 76	20-49 (n = 34); 50-69 (n = 115); 70-89 (n = 90)	Asian	71.5%; 61.5%; 59.8%; 59.4%; 53.6%; 48.1%; 38.1% (N/A, D)	[82]
182	40.1%	147~200	61.2±14.2	Mostly White	82% (A; S)	[83]
140	61.0%	N/A	74.1±6.6	Amerindians (n = 70) European ancestry (n = 70)	60% (O; D)	[84]
92	38.0%	N/A	64.0±9.5	Mostly Asian	65.8% (A; D)	[85]
90	51.1%	100	57.1±11.7	White (n = 66); Black (n = 19); Hispanic (n = 5)	88.9% (A; D)	[86]
36	47.2%	100~370	52.92±18.74	White (n = 15); Asian (n = 13); Black (n = 5); Hispanic/Latino (n = 3)	75.3% for conventional rigid probe; 70.6% for our patch (A; D)	This study

A, adequate signal, including optimal and suboptimal signals (for example, only part of the arterial segments cannot be accessed); D, double sides of the temporal window; N/A, not available; O, optimal signal; S, single side of the temporal window. This table summarizes findings from various studies on the success rate of the TCD examination across different demographic groups and applied acoustic intensities. Each study is categorized by the number of participants, sex distribution, applied acoustic intensity, age distribution, race/ethnicity of the study population, and the reported success rate. The last row presents aggregated data from this study, highlighting the similar success rates of this study to the published ones. References 73–86.